TUDelft

Delft University of Technology

Control recovery of a satellite with flexible appendages after space debris impact

Gransden, Derek I.; Mooij, E.

Important note
To cite this publication, please use the final published version (if applicable).
Please check the document version above.

AIAA-18-2099

Control Recovery of a Satellite with Large Flexible Appendages after Impact with Space Debris

D.I. Gransden and E. Mooij
Delft University of Technology, Delft, The Netherlands

AIAA Spaceflight Mechanics Conference/
AIAA Guidance, Navigation, and Control Conference
January 8-12, Kissimmee, FL

Control Recovery of a Satellite with Flexible Appendages after Space Debris Impact

Derek I. Gransden[*] and Erwin Mooij[†]

Delft University of Technology, Faculty of Aerospace Engineering,

Kluyverweg 1, 2629 HS Delft, The Netherlands

Larger power requirements from modern spacecraft precipitate enormous solar arrays to fulfil budgetary needs. Although the solar arrays may have a relatively small influence on the total mass of the spacecraft system, large arrays with long flexible panels do affect the dynamics of the satellite bus through the Steiner terms in the moments of inertia. Unfortunately, such large arrays are broad targets for incoming orbital debris, and impacts are an increasing risk to attitude control and during guidance operations. This paper examines the effect of impacts on the response of a Rosetta-like spacecraft controlled by an adaptive controller. The control system design is based on simple adaptive control theory, and uses a stabilised, linear reference model to swiftly drive the plant output error to zero and hence achieving a commanded attitude. The adaptive controller is tuned using a linearised Euler-Bernoulli beam model as a computationally inexpensive flexible system. The elastic dynamics increases the controller effort and shows the effect of the elastic bodies on the controller system by the deviations from an implementation for a rigid satellite only. A sample investigation of an impulsive force, simulating a particle debris impact, shows the control effort exerted to stabilise the spacecraft. Additional simulations covering a range of particle momenta and impact location on the spacecraft show controller efforts for a satellite in a steady-state configuration and undergoing a three-axis manoeuvre. For individual impact cases, the controller shows a robust performance, even if there is some initial saturation of the actuators. In multiple impact scenarios, the control effort is much heavier and strong oscillatory behaviour is observed, indicating the limits of the controller.

I.   Introduction

Spacecraft operating in the inner part of the Solar System commonly rely on photovoltaic solar panels to derive electricity from sunlight. This is a reliable and relatively inexpensive way to accommodate the power requirements. Power requirements on satellites seem to be becoming more demanding, driving the dimensions of the solar panels. A typical and well-known example is the International Space Station (Fig. 1) with its largest panels being about 33 m × 4.5 m a piece. While manoeuvring such a large system, one needs to consider the dynamical properties of these panels as well as other appendages, and make sure they do not affect the stability and controllability of the complete system. Fortunately, due to the large inertia of such a space station, the effects may be limited when properly considered.

However, smaller (and much lighter) satellites may have large power demands as well. A good example is the category of communications satellites, with, for instance, panel lengths of about 19 m for the next generation of Intelsat satellites (Intelsat 29e, launched early 2016, spans a total of 44 m), or the total deployed length of 40.9 m of the HS-702 satellite bus of Hughes Space and Communications Company. Another example of large solar panels is the Earth-observation satellite Envisat, with a single panel of 14.2 m× 5 m mounted on a meters-long extension rod.

Having large, flexible appendages may induce unwanted oscillations when (sudden) attitude changes occur, either originating from the control system for mission-specific reasons or, for instance, when small

---

[*]Assistant Professor, Section Structural Integrity & Composites, d.i.gransden@tudelft.nl.

[†]Assistant Professor, Section Astrodynamics and Space Missions, e.mooij@tudelft.nl, Associate Fellow AIAA.

Figure 1. International Space Station with its array of large solar panels. Image courtesy: NASA

space-debris particles hit one of the solar panels. Robust control algorithms that can counteract these unmodelled dynamics may be the solution to guarantee the stability of the satellite. One possible candidate for such a robust control system is one based on model reference adaptive control (MRAC), and more specifically the simple adaptive control (SAC) theory developed in Ref. 1, which has shown a variety of applications in the field of robotics,[2] autopilot design,[3] space-telescope control,[4] and entry systems.[5]

Reference 6 discussed the real-time implementation of SAC for the attitude control of a satellite with large, rigid solar panels. The current paper aims to follow up on that work by looking at the influence of large, flexible solar panels on the performance of the adaptive controller. The key aspect here is to see the effect of flexibility without having to change the controller developed for the rigid satellite. As a test case, the Rosetta-like spacecraft with similarly sized solar panels is used, although without any particular mission in mind.

The remainder of this paper is organised as follows. Section II describes, with references to previous works, the theory and modelling aspects of flexible solar panels using flexible beam elements. Section III provides, after a brief background on simple adaptive control, a detailed overview of the control-system design and the benchmark results for a manoeuvring flexible satellite. In Sec. IV, the results for a battery of impact simulations are reviewed with respect to the control and accuracy of the satellite orientation. Section V concludes the paper and provides some recommendations.

II. Satellite Structural Model

Work on articulated rigid body satellites with flexible multi-body appendages can be found, for instance, in Ref. 7, where the authors treat two different approaches: a Newtonian mechanics rigid body method and flexible motion treated with Lagrange equations and implemented with a finite element (plate) method. Stability analyses have also been performed for a rigid satellite bus coupled with solar arrays.[8] They show that flexible panels do influence the stability margins of the satellite, but the choice of modelling techniques may also influence its stability margins. Flexible solar arrays are commonly modelled as beams, in a finite element software to determine the mode shapes, and applied to the state-space as normalised co-ordinates.[9,10,11]

In this work, the intention is to create a simplified structural model to replace the slower three-dimensional hexahedral model with constrained rigid body and elastic body mechanics used in previous research,[12,13] which will be compared in a future paper. With a faster model, a comparison between a simplified linear model and a complex nonlinear model can be made to determine how the modelling technique influences the stability of the spacecraft. A computationally fast model with simplified geometry can be used to tune the adaptive controller and a more robust, more accurate, but more computationally expensive model can replace the simplified model when performing system-wide verification and validation.

Therefore, a linear, two node-per-element, three-dimensional Euler-Bernoulli beam model replaces the former to allow fast sensitivity and controller verification with respect to variable geometric and material properties. The beam model is separated into three physical parts: the flexible solar panels, a rigid-like link that separates the solar panels from the satellite bus, and the satellite bus itself. The three parts are exactly
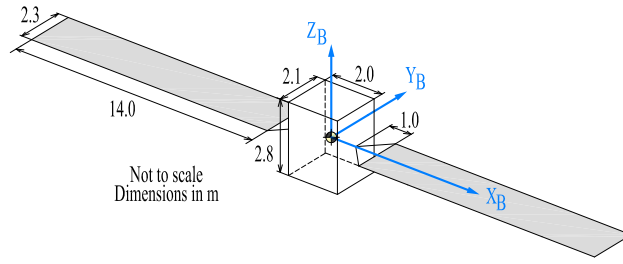
Figure 2. Satellite Geometry.

as described in Ref. 13; but Fig. 2 shows the global co-ordinate system and satellite geometry. However, in place of the constrained mechanics of the previous work, a continuous beam model is presented such that the satellite bus and links are represented together, without the use of Lagrange multipliers that may destabilise the simulation.[14]

Euler-Bernoulli beam models are common in finite element mechanics texts, although it is more difficult to find three-dimensional beam models. For a three-dimensional development of a beam model, a reader is referred to Ref. 15 and extending models found in Ref. 16 as examples. In Ref. 18, the matrices are presented in their full form for clarity. These matrices depend only on the material properties of the beam, the Young's modulus (E), the shear modulus (G), and its density (ρ); and the geometric properties defining the beam's resistance to forces and moments, the area (A), and the second (and polar) moments of area (I_y, I_z, and J). It must be mentioned that the beam element properties depend on the location of the element with respect to the satellite, that is, the material and geometric properties listed are consistent with part of the satellite upon which the element exists. Therefore, the values of E, G, ρ, A, I_y, I_z, and J depend on its location in the beam model: whether the element is part of the satellite bus, the connecting link, or the solar panels.

The beam model uses a set of Tait-Bryan angles as a directional cosine matrix for the orientation of the deformed beam. In the initial configuration, the beam model is coincidental with the inertial X-axis. Figure 3 shows a beam element with Nodes 1 and 2, in the deformed configuration with respect to the inertial co-ordinate system. (Note: the directional rotation angles do not, in general, correspond to the Euler angles used for the controller. The transformation matrix is the multiplication of the rotation about the x-, y-, and z-axes.) Elemental positive directions are initially assumed to be co-linear with the inertial co-ordinate system.

The global mass and stiffness matrices, $\mathbf{M}$ and $\mathbf{K}$, are assembled using the transformation

$$\mathbf{M} = \mathbf{R}^\mathsf{T} \mathbf{m}_e \mathbf{R} \tag{1}$$

$$\mathbf{K} = \mathbf{R}^\mathsf{T} \mathbf{k}_e \mathbf{R} \tag{2}$$

Figure 3. Beam Geometry.

American Institute of Aeronautics and Astronautics
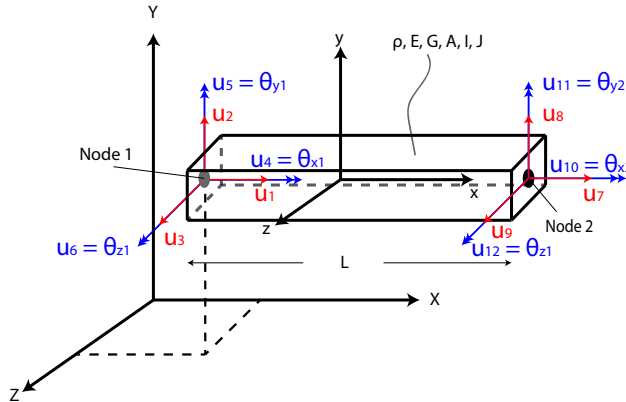
where the elemental mass and stiffness matrices, $\mathbf{m}_e$ and $\mathbf{k}_e$, are composed of the material and geometric properties listed above, and the global rotational matrix, $\mathbf{R}$ is

$$\mathbf{R} = \begin{bmatrix} \mathbf{r} & 0 & 0 & 0 \\ & \mathbf{r} & 0 & 0 \\ & & \mathbf{r} & 0 \\ \text{sym.} & & & \mathbf{r} \end{bmatrix} \tag{3}$$

and similarly $\mathbf{r}$ is the product of the intrinsic rotation matrices

$$\mathbf{r} = \mathbf{X}(\theta_x)\,\mathbf{Y}(\theta_y)\,\mathbf{Z}(\theta_z) \tag{4}$$

Therefore, once the nodal displacements have been calculated, the internal (elemental) forces and moments can be recovered as

$$\mathbf{F}_e = \mathbf{k}_e \mathbf{R} \mathbf{d}_e \tag{5}$$

The elemental force and displacement vectors are given as

$$\mathbf{F}_e = \begin{bmatrix} F_x^{(1)} & F_y^{(1)} & F_z^{(1)} & M_x^{(1)} & M_y^{(1)} & M_z^{(1)} & F_x^{(2)} & F_y^{(2)} & F_z^{(2)} & M_x^{(2)} & M_y^{(2)} & M_z^{(2)} \end{bmatrix}^{\mathsf{T}} \tag{6}$$

and

$$\mathbf{d}_e = \begin{bmatrix} d_x^{(1)} & d_y^{(1)} & d_z^{(1)} & \theta_x^{(1)} & \theta_y^{(1)} & \theta_z^{(1)} & d_x^{(2)} & d_y^{(2)} & d_z^{(2)} & \theta_x^{(2)} & \theta_y^{(2)} & \theta_z^{(2)} \end{bmatrix}^{\mathsf{T}} \tag{7}$$

where the superscript denotes the element nodal number.

These matrices are assembled in the same manner as the solid body elastic mechanics, which will have the generic form (since a damping ratio is not currently used):

$$\mathbf{M}\ddot{\mathbf{d}} + \mathbf{K}\mathbf{d} = \mathbf{F} \tag{8}$$

The time integration is done by Newmark's method, which allows one to have second-order accuracy for a spectral radius, $\rho_\infty = 1.0$, and is stable under the conditions

$$\gamma \geq \frac{1}{2}, \qquad \beta \geq \frac{1}{4}\left(\gamma + \frac{1}{2}\right)^2$$

So, for each time step one can rewrite Eq. (8) as

$$\mathbf{M}\mathbf{a}_{n+1} + \mathbf{K}\mathbf{d}_{n+1} = \mathbf{F}(t_{n+1}) \tag{9}$$

where according to Newmark's method, updating the acceleration and velocity is,

$$\left.\begin{aligned} \mathbf{a}_{n+1} &= \frac{1}{\beta\Delta t^2}(\mathbf{d}_{n+1} - \mathbf{d}_n) - \frac{1}{\beta\Delta t}\mathbf{v}_n - \frac{1-2\beta}{2\beta}\mathbf{a}_n \\ \mathbf{v}_{n+1} &= \mathbf{v}_n + \gamma\Delta t\mathbf{a}_{n+1} + (1-\gamma)\Delta t\mathbf{a}_n \end{aligned}\right\} \tag{10}$$

Now that all unknowns can be described using only the unknown displacements, $\mathbf{d}_{n+1}$, by taking the Gateaux derivative, and rearranging so that the unknown displacements are on the left side of the equation,

$$\left\{\frac{1}{\beta\Delta t^2}\mathbf{M} + \mathbf{K}\right\}\mathbf{d}_{n+1} = \frac{1}{\beta\Delta t^2}\mathbf{M}\mathbf{d}_n + \frac{1}{\beta\Delta t}\mathbf{M}\mathbf{v}_n + \frac{1-2\beta}{2\beta}\mathbf{M}\mathbf{a}_n + \mathbf{F}(t_{n+1}) \tag{11}$$

$$\mathbf{K}_{\text{effdyn}}\mathbf{d}_{n+1} = \mathbf{F}_{\text{effdyn}}(t_{n+1}) \tag{12}$$

which is solved as usual. With $\mathbf{d}_{n+1}$ known, one can solve for the unknown velocities and accelerations using Eq. (10).
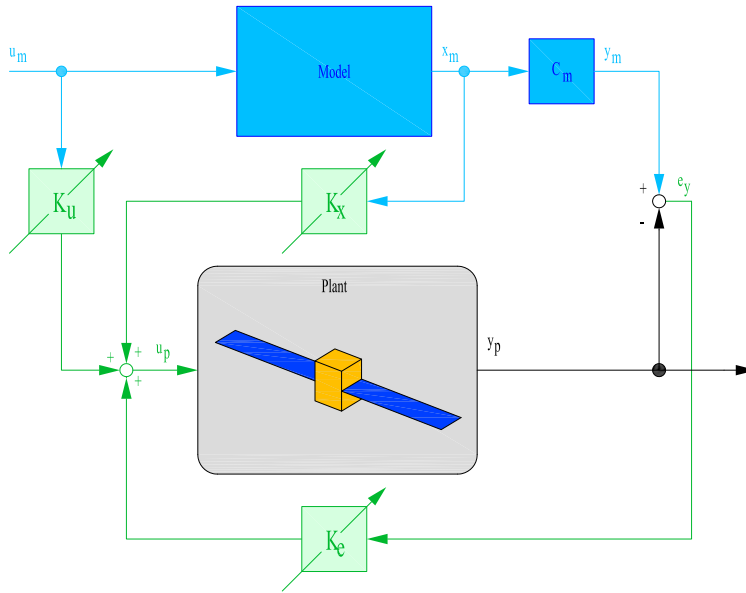
Figure 4. Basic architecture of a Simple Adaptive Control algorithm.

III. Control System Design

A. Simple Adaptive Control

The attitude-control system is developed using the concept of so-called simple adaptive control (SAC),[1] and is based on the principle of tracking the output of a reference model. Therefore, this system could also be classified as a model reference adaptive control (MRAC) system, although a principal difference from the original MRAC is that full state knowledge of the plant to be controlled is not required. A schematic overview of a simple adaptive controller is shown in Fig. 4. The control law is given by

$$\mathbf{u_p}(t) = \mathbf{K_r}(t)\mathbf{r}(t) \tag{13}$$

where $\mathbf{r}(t) = [\mathbf{e_y}(t) \; \mathbf{x_m}(t) \; \mathbf{u_m}]^\mathsf{T}$ and $\mathbf{K_r}(t) = [\mathbf{K_e}(t) \; \mathbf{K_x}(t) \; \mathbf{K_u}(t)]$. It can be seen that the model input $\mathbf{u_m}$ and model state $\mathbf{x_m}$ are required to form part of the input signal $\mathbf{u_p}$ to the plant. Moreover, the so-called output error $\mathbf{e_y}$ serves as a feedback quantity to form the third element that composes $\mathbf{u_p}$. The three gains, *i.e.*, $\mathbf{K_x}$, $\mathbf{K_u}$ and $\mathbf{K_e}$, are adaptive.

To compute the adaptive gains, $\mathbf{K_r}$ is defined to be the sum of an integral and a proportional component:

$$\mathbf{K_r}(t) = \mathbf{K_i}(t) + \mathbf{K_p}(t) \tag{14}$$

with

$$\dot{\mathbf{K}}_\mathbf{i}(t) = \mathbf{e_y}\mathbf{r}^\mathsf{T}(t)\mathbf{T_i} \tag{15}$$

$$\mathbf{K_p}(t) = \mathbf{e_y}(t)\mathbf{r}^\mathsf{T}(t)\mathbf{T_p} \tag{16}$$

In Eqs. (15)-(16), the weighting matrices $\mathbf{T_p}$ and $\mathbf{T_i}$ are positive semi-definite and positive definite, respectively. Note that the proportional-gain component has a direct influence on the transient tracking behaviour, but is strictly speaking not required to enforce asymptotic tracking, as $\mathbf{T_p}$ can be zero. This is guaranteed by the integral gain. To improve the transient response by only using an integral gain, a constant gain value can be added to $\mathbf{K_i}$. An advantage over the use of the proportional gain is that this constant value is independent of $\mathbf{e_y}$, and is therefore non-zero even if $\mathbf{e_y}$ is zero. In that case, the integral gain derived from Eq. (15) becomes

$$\mathbf{K_i}(t) = \mathbf{K_{i,0}} + \int_0^t \dot{\mathbf{K}}_\mathbf{i}(t)\mathrm{d}t \tag{17}$$

One way to improve the damping of the system is to include the error derivatives in the output error vector. In that case, the error for output $\mathbf{y}$ becomes:

$$\mathbf{e_y}(t) = \mathbf{K_y^\mathsf{T}}(\mathbf{y_m}(t) - \mathbf{y_p}(t)) + \mathbf{K_{\dot{y}}^\mathsf{T}}(\dot{\mathbf{y}}_\mathbf{m}(t) - \dot{\mathbf{y}}_\mathbf{p}(t)) \tag{18}$$

with $\mathbf{K_y^\mathsf{T}}$ and $\mathbf{K_{\dot{y}}^\mathsf{T}}$ being a proportional and derivative output gain, respectively. However, to avoid calculating the numerical derivative of the outputs and to tune the related gains in multiple-output systems an alternative expression for the output error may be used. Adjusting the output matrix by pre-multiplying it with $\mathbf{K_c}$, the optimal gain matrix from solving the Algebraic Riccati Equation for a closed-loop linearised version of the plant, sufficient damping is commonly introduced in the system to have a proper response.[17] The output error becomes in that case

$$\mathbf{e_y} = \mathbf{y_m} - \mathbf{y_p} = \mathbf{K_c}\left(\mathbf{C_m}\mathbf{x_m}(t) - \mathbf{C_p}(\mathbf{x_p}, t)\mathbf{x_p}(t)\right) \tag{19}$$

So far, an ideal environment has been considered. To cope with environmental disturbances that lead to a persistent non-zero error and therefore to a continuous change in the integral gain $\mathbf{K_i}$, a robust design can be applied to adjust the integral gain and preventing it from reaching very high values. The integral term of Eq. (15) is adjusted as follows:

$$\dot{\mathbf{K}}_\mathbf{i} = \mathbf{e_y}(t)\mathbf{r}^\mathsf{T}\mathbf{T_i} - \sigma_i\mathbf{K_i}(t) \tag{20}$$

Without the σ_i-term, $\mathbf{K_i}(t)$ is a perfect integrator and may steadily increase (and even diverge) whenever perfect output-following is not possible. Including the σ_i-term, $\mathbf{K_i}(t)$ is obtained from a first-order filtering of $\mathbf{e_y}(t)\mathbf{r}^\mathsf{T}\mathbf{T_i}$ and, therefore, cannot diverge, unless the output error diverges.

B. Reference Model

The current application of SAC focuses on a satellite with two large solar panels, and has been schematically depicted in Fig. 2. Whereas an actual satellite consists of a rigid bus with two flexible solar panels, the reference model for the controller is assumed to be a linearised, rigid satellite. This choice should make it possible to obtain a more or less rigid-body response for an actual satellite if strict model-following is achieved.

The geometry and mass properties of the rigid satellite have been defined such that they match those of a Rosetta-like satellite.[13] The satellite body is a parallelepiped with a height of 2.8 m, and a rectangular top and bottom cover of 2.1 m × 2.0 m. The mass of this body is 2,030 kg (dry mass plus current fuel; fuel sloshing is not considered, though), assumed to be uniformly distributed, with a corresponding inertia tensor of $\mathbf{I_{bus}} = \mathrm{diag}(1991,1924,1364)$ kg m^2. The two solar panels are represented by rectangular flat plates of 14 m × 2.3 m, each having a mass of 40 kg and an inertia tensor of $\mathbf{I_{panel}} = \mathrm{diag}(18,653,671)$ kg m^2, referenced to the panel centre of mass, which is located at half the panel length.[a] In the current simulation model, the panels are fixed to the satellite body with a stiff connection of 1 m, transferring forces and moments at a point on the related wall, located at the geometric centre of the satellite bus face. The inertia tensor for the complete (rigid) system is $\mathbf{I_B} = \mathrm{diag}(2027,9746,9150)$ kg m^2. The satellite's position is currently of no importance as neither the flight environment nor any coupling with the orbital motion is considered. Actuators for this satellite include a set of reaction control system (RCS) thrusters, with maximum available moments of $M_T = \pm 50$ Nm around each axis.

The reference model consists of a linearised state-space model for the rotational motion of the satellite, based on Euler angles for the attitude representation, $i.e.$,

$$\dot{\mathbf{x}}_\mathbf{m} = \mathbf{A_m}\mathbf{x_m}(t) + \mathbf{B_m}\mathbf{u_m}(t) \qquad \mathbf{y_m} = \mathbf{C_m}\mathbf{x_m}(t) \tag{21}$$

with the model state and control vector given by

$$\mathbf{x_m} = \begin{pmatrix} p_m & q_m & r_m & \phi_m & \theta_m & \psi_m \end{pmatrix}^\mathsf{T} \qquad \mathbf{u_m} = \begin{pmatrix} M_{Tm,x} & M_{Tm,y} & M_{Tm,z} \end{pmatrix}^\mathsf{T}$$

and the model output vector $\mathbf{y_m}$ defined by the reference-model related part of Eq. (19), $i.e.$,

$$\mathbf{y_m} = \mathbf{K_c}\mathbf{C_m}\mathbf{x_m}(t)$$

---

[a]The tensor is defined with respect to a local panel frame, with the X-axis pointing outwards along the panel centre line, the Y-axis parallel to the Y_B-axis, and the Z-axis being the right-handed complement.

American Institute of Aeronautics and Astronautics

Table 1. Design parameters roll controller

	T_p	T_i	$K_{i,0}$	σ_i
e_ϕ	10	15	80	0.2
p_m	10,000	20,000	100	0
ϕ_m	8,000	8,000	100	0
$M_{Tm,x}$	0.5	0.05	-1	0

Table 2. Design parameters pitch controller

	T_p	T_i	$K_{i,0}$	σ_i
e_θ	8	6	6	0.2
q_m	10,000	10,000	0	0
θ_m	8,000	8,000	0	0
$M_{Tm,y}$	0.005	0.01	0	0

Table 3. Design parameters yaw controller

	T_p	T_i	$K_{i,0}$	σ_i
e_ψ	10	15	100	0.2
r_m	10,000	20,000	2	0
ψ_m	8,000	8,000	2	0
$M_{Tm,z}$	0.05	0.03	-1.5	0

The above satellite model is stabilised by means of a linear quadratic regulator (LQR), *i.e.,* a linear state-feedback controller for which the gains, $\mathbf{K_c}$, have been computed with optimal control theory.[19] Input for the design of the LQR is the maximum allowable state deviation and the maximum control effort. The applied numerical values are $\Delta p_{max} = \Delta q_{max} = \Delta r_{max} = 0.2°/s$ and $\Delta\phi_{max} = \Delta\theta_{max} = \Delta\psi_{max} = 0.5°$ for the state variables, and $\Delta M_{Tx,max} = \Delta M_{Ty,max} = \Delta M_{Tz,max} = 50$ Nm for each of the control parameters. The low values for the angular-rate deviation should prevent actuator saturation, as the (heavy) satellite might be slow to start rotating. The small values for the angle deviations, on the other hand, would lead to slightly larger actuator commands such that the control will be "tighter". In terms of gain values, the ones associated with the angular rate carry more weight.

The given values for the maximum state deviation should not be confused with the pointing error. These values mean that if an angle error larger than these values occurs, the LQR controller will command maximum thrust to bring the error back to values lower than those. Of course, the steady-state condition is ideally a zero-error state, and the LQR is capable to get very close to that. The SAC will, of course, follow and in that way a small pointing error is obtained. To start the controller design from actual requirements on pointing accuracy is currently beyond the scope of the research and remains to be done as future work.

C. Integrated System

The reference model is used in such a way that, when the commanded attitude changes, the effect is immediately noticeable, and the closer the reference model approaches the commanded attitude, this effect will diminish. So rather than *following* the command, it will try to reduce the *difference* between plant state and command. For example, when a one-degree step is applied to any of the attitude angles, the corresponding model angle will develop a one-degree error that the stabilising LQR tries to reduce to zero. Since the corrective control will be large when faced with this error, it provides a strong reference signal to the adaptive controller. Any successive change in command will then be added as a differential error with respect to the previous command. The advantage of this implementation is that a maximum transient response is enforced right from the beginning, taking all information from the model into account. When the plant state approaches the commanded value, and the model has returned to its nominal state, the driving signal will be the output error, $\mathbf{e_y}$, and can be considered as a fine tuning of the response that removes the steady-state error. An additional advantage is that when in steady state, the input signals from the model are zero, and thus cannot result in jittering when a small output error occurs.

The design parameters of the adaptive controller are the weighting matrices, $\mathbf{T_p}$ and $\mathbf{T_i}$, the initial values of the integral gain, $\mathbf{K_{i,0}}$, and, as a safeguard against diverging output errors, the filter parameter, σ_i. Because the satellite is heavy and the response is expected to be relatively slow, the three axes of motion are considered to be decoupled, and each of the attitude angles will be controlled separately. A baseline controller has been developed in Ref. 18 and will be used in this paper; the design parameters are listed in Tables 1-3.
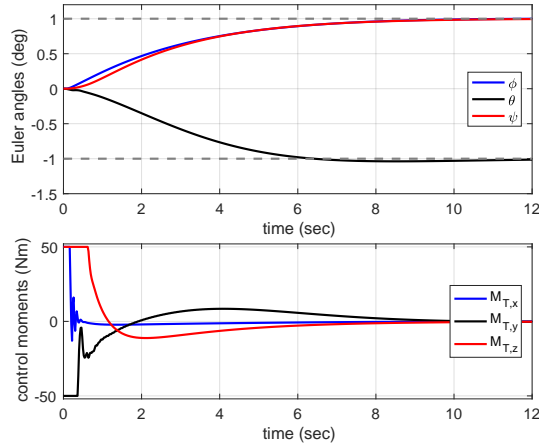
American Institute of Aeronautics and Astronautics

Figure 5. Nominal response for combined step commands.

Table 4. Design parameters output-error controller

	T_p	T_i	$K_{i,0}$	σ_i
e_ϕ	5	5	1	0.2
e_θ	10	10	2	0.5
e_ψ	5	5	1	0.2

As an example of the nominal response of the satellite using the baseline controller, commanded steps of $\phi_c = \psi_c = 1°$ and $\theta_c = $ -1° are executed at $t = 0$ s. Figure 5 shows the time history of the three Euler angles obtained with the adaptive controller. For both ϕ and ψ it takes about 10 s to execute the command; the pitch response is a bit faster, even though this axis is the more difficult one to control. In the lower part of the figure, the corresponding control moments are plotted. As the controller is designed for accurate "pointing", allowing only small errors after a brief transient period, the thrusters are momentarily saturated. Once the satellite starts rotating the thruster moments quickly reduce.

The above response is an example of a controller that receives commands to follow. However, once in steady-state the reference model will no longer act as a signal generator to the adaptive-gain algorithm, because the reference model is no longer commanded to do anything, except to remain at rest. The output of the reference model is thus zero. The moment a perturbation drives the satellite away from the steady-state, the controller will command the system back to the original steady-state. Since the reference model is already in that state, the only signal that can drive the gain algorithm is the output error, *i.e.*, the difference between satellite state and the reference model, of which the output is zero. Thus, in that case pure output-error control is performed. However, since the gain algorithm has been tuned expecting all signals to be non-zero, the controller performance will degrade. Therefore, it makes sense to have a second set of weighting matrices for perturbation control, when no (additional) manoeuvre is commanded. Parameters that provide an acceptable performance are listed in Table 4. It is noted that the scaling gain, $\mathbf{K_c}$, in Eq. (19) has to be adapted with Δq_{max} 0.5°s and $\Delta\theta_{max} = 1°$ to avoid premature saturation of the controls.

IV.   Results

In this section the effect of space-debris impact on the satellite control are analysed. It is assumed that debris particles impact with the solar panels and transfer momentum to the system. The change in angular momentum causes the satellite to rotate and induce control errors that are subsequently reduced to zero by the controller. To be able to study different aspects, Sec. IV.A introduces an uncontrolled impact to show the flexible mechanics. In Sec. IV.B a number of performance indicators are introduced. Next, Sec. IV.C discusses the effect of an impact for both an uncontrolled and a controlled satellite, as well as the case where the satellite is performing manoeuvres. Finally, in Sec. IV.D the results of extensive Monte-Carlo analyses are presented.

American Institute of Aeronautics and Astronautics

A.   Flexible Satellite Verification

To compare the satellite natural frequencies and displacements under impact or rotational loading, a finite element model was also created in Dassault Systèmes Abaqus®. Both models, which will be referred to as the simplified model and the commercial model, were created in the same manner: a connected set of elements representing the span of the satellite from the solar panels, the connecting link, and the satellite bus, with the appropriate symmetry. Both models have 80 elements spanning each of the solar panels, each rigid link has 1 element, and the satellite bus consists of 2 elements, for a total of 164 elements and 990 degrees of freedom.

Both models have the same geometric and material properties, as shown in Table 5. In this table the labels m_{sp}, m_{bus}, and m_{link} refer to the masses of each of the solar panels, the satellite bus, and each of the connecting links, respectively. The total mass of the satellite is given by m_{tot} and the mass moments of inertia I_{xx}, I_{yy}, and I_{zz} are also for the entire satellite. Both models' flexibility parameters are based upon an estimated 1 Hz cantilever-beam first natural frequency. The natural frequencies of both models are listed in Table 6.

The differences in the natural frequencies can perhaps be explained by the default use of Timoshenko elements in the commercial model, although with a correction for the slenderness ratio, and the fact that the commercial model uses fewer assumptions regarding the reduction in dimensionality of the physical system. (For example, in the simplified model shear and warping effects are neglected and bending loads do not contribute to the extension or contraction of the beam.) It should be noted that the eigenmodes of the two models are identical for symmetric modes and vary slightly (a larger slope of the satellite bus orientation in the commercial model) in the anti-symmetric modes. Since the mass properties of the two models are nearly identical, varying by less than 3% in the case of I_{yy}, it seems the main contribution for the differences of the natural frequencies arises from the stiffnesses, and the stiffness of the commercially generated model must be lower for anti-symmetric cases. The effective Young's moduli are chosen to be the same for each partition of the beam: the solar panels, the connecting links, and the satellite bus; therefore, this must come from the additional contributions of a more rigourous model in the commercial software. It would seem to support the fact that the rotations of the satellite hub in the anti-symmetric modes are due to shear effects that are not considered in the simplified model. (Additionally, the simplified model does not support large rotations, which limits the validity of the model.) These effects are also apparent on the displacement of the longitudinal co-ordinate.

In the beam model verification, no damping is desired so the Newmark's method parameters are $\rho_\infty = 1.0$, $\beta = 0.25$, and $\gamma = 0.5$, but the commercial model uses the defaults in the explicit-dynamic solver. There is a difference in the time step between the two models: the simplified model uses a $\Delta t = 0.002$ s (an order of magnitude lower than the nominal control simulations), but the commercial model automatically calculates the largest stable time step available for the explicit solver, which was found to be $\Delta t = 5 \times 10^{-8}$ s. Therefore, the computational time for both models is also not equivalent. To test the simplified model, and to connect the research with a paper related to orbital control with low-momentum impacts concurrently presented with this one, an impact of an object with the spacecraft is simulated. Both models (simplified and commercial) are run with an impact of 100 N, uncontrolled, in the z- and y-directions for a duration of

Table 5.   Mass properties of simplified model and commercial model

	m_{tot} kg	m_{sp} kg	m_{bus} kg	m_{link} kg	I_{xx} kgm^2	I_{yy} kgm^2	I_{zz} kgm^2
Simplified	2030	40	1950	0.1	2027	9746	9150
Commercial	2030	40	1950	0.1	2026	10036	9154

Table 6.   Natural frequencies of the simplified model and commercial model

	1st	2nd	3rd	4th	5th	6th
Simplified [Hz]	1.029	2.653	6.395	7.858	17.86	18.79
Commercial [Hz]	1.029	1.925	6.394	6.867	17.86	18.12
% Difference	0.000	31.80	0.000	13.46	0.000	0.04

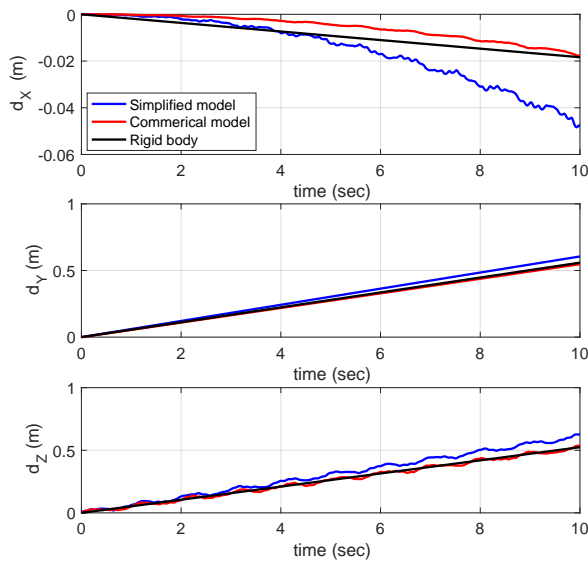American Institute of Aeronautics and Astronautics

Figure 6. Starboard edge displacements of both models and rigid body motion during impact and drift phases of the simulation.
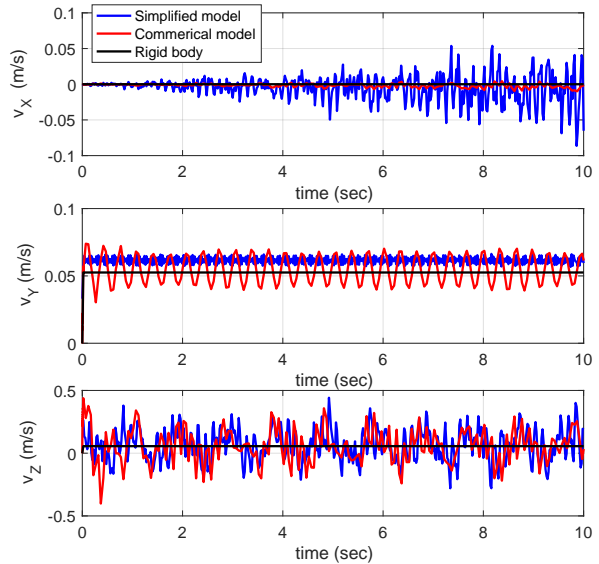

Figure 7. Starboard edge velocity of both models and rigid body motion during impact and drift phases of the simulation.

Table 7. Comparison of the tip displacement after 10 s of uncontrolled drift

	d_x	d_y	d_z
Simplified [Hz]	-0.0475	0.605	0.629
Commercial [Hz]	-0.0177	0.547	0.537
% Difference	91.4	10.1	15.8

0.02 s, and left to drift for the remaining time up to 10 s at which time the simulation ends.

An impact and drift simulation is conducted of an impulsive change in angular momentum of the satellite bus due to the impact of a space-debris particle. A mass of 1 g was assumed to impact the solar panel with a differential velocity of 2 km/s in Y- and Z-directions. Assuming that the linear momentum is transferred in 0.02 s this implies a force of $F_Y = F_Z = 100$ N. The impact point is taken along the centreline of the panel at its outboard tip, yielding a moment arm of 16.0 m; thus a moment of $M_Y = 1,600$ Nm (for the duration of 0.02 s).

The results of the impact simulation on the two models shows some differences, in particular in the starboard solar panel edge displacement and velocity. These two indicators were chosen because they give the greatest deviation from the rigid body deflections and are also closely related to the values the controller uses, which are the angles and angular velocities of the satellite bus. Figure 6 shows the tip displacements of the starboard solar panel edge as a function of time and the rigid body tip displacement is included to show what the rotational displacement would be in case the stiffnesses were infinite. The final tip displacement is compared in Table 7, with the rigid tip displacement given as well. Clearly, the rigid tip displacement is not meant to be compared to the elastic body displacements; however, it is useful to see the effect of the rigidity of the panels, given that the moments of inertia are greater in the y-direction than in the z-direction.

Figure 6 shows that there is an approximately constant discrepancy between the simplified model and the commercial model, but otherwise the vibratory motion of the solar panels is reasonably well captured. For each direction, the same period and amplitude of elastic motion is found for the flexible bodies, although it is not clear for the y-direction. The x-axis displacement has a non-constant error due to the combined effect of the additional displacement of the y- and z-axes. Figure 7 shows the starboard edge velocity during the simulation time, and it is clear that the discrepancy in the displacement variables comes from the differences in velocity. While the commercial solver edge velocities oscillate around the rigid body velocities, the simplified model velocities are offset. This is particularly visible in v_y, in which high frequency but small amplitude vibrations dominate the elastic response. Table 7 summarises the differences between the end-time tip displacements of both models.
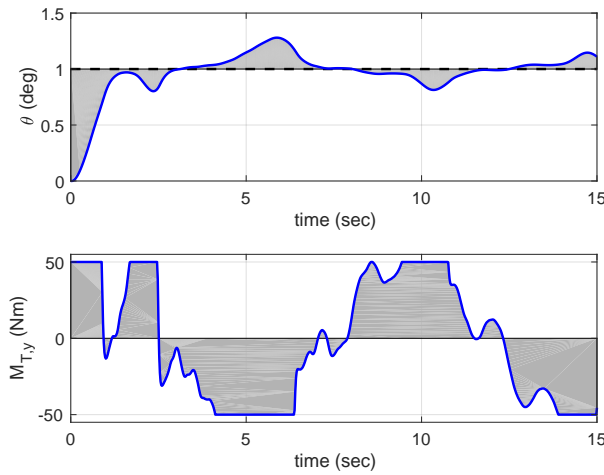
American Institute of Aeronautics and Astronautics

Figure 8. Controller performance indices: integrated control error (top) and control effort (bottom).

Despite the differences between the simplified model and the commercial software, it does indicate that the simplified model reasonably calculates displacements that are on the correct order and it is computationally inexpensive, compared to a full three-dimensional continuum or commercial software model. For the remaining impact simulations, some small measure of numerical damping is included, so the Newmark's method parameters are $\rho_\infty = 0.95$, $\beta = 0.263$, and $\gamma = 0.5256$. These parameters are chosen to reduce the undesirable numerical high frequency oscillations in the solution that cause the controller to over-correct and become unstable. Additionally, the time step, a $\Delta t = 0.02$ s is used in the remaining simulations.

B. Performance Analysis

The performance of a controller can be derived from several defined objective functions. For the current control-system design, one may look at the minimum state deviation of the satellite (or the plant) with respect to the guidance commands. Another objective in the design could be to minimise the control effort that is required to influence the plant's behaviour. For the current satellite-control problem, these two objective functions can be expressed as the integrated Euler-angle deviation and the integrated thruster activity (the total amount of fuel, or, equivalently, the required control moments), given by:

$$\sum_{\phi_{err}} = \int_0^t |\phi_c(t) - \phi_p(t)| \mathrm{d}t \qquad \sum_{\theta_{err}} = \int_0^t |\theta_c(t) - \theta_p(t)| \mathrm{d}t \ \phi \qquad \sum_{\psi_{err}} = \int_0^t |\psi_c(t) - \psi_p(t)| \mathrm{d}t \qquad (22)$$

$$\sum_{M_{T,x}} = \int_0^t |M_{T,x}(t)| \mathrm{d}t \qquad \sum_{M_{T,y}} = \int_0^t |M_{T,y}(t)| \mathrm{d}t \qquad \sum_{M_{T,z}} = \int_0^t |M_{T,z}(t)| \mathrm{d}t \qquad (23)$$

A graphical representation of the above metrics is shown in Fig. 8, represented by the grey areas, for a step command in the pitch angle when thruster control is used to follow this command. It is obvious that both individual areas should be as small as possible for optimal controller performance, which means they can be used to evaluate different controller designs. In the given example, $\sum_{\theta_{err}} = 1.738°$s and $\sum_{M_{T,y}} = 523.3$ Nm s.

Note that for the sake of this example the controller performance has been significantly downgraded (large pitch-rate gain for a satellite with very flexible solar panels).

To detect oscillations or otherwise discrete changes in the controls, the cumulative moving standard deviation can be used. For a subset j of n_s out of a total of N samples of an arbitrary control signal u, the moving mean is defined as $\bar{y}_j = \frac{1}{n_s} \sum_{i=j}^{j+n_s-1} u_i$. Here, j will run from $j = 1+n_s/2$ to N-$n_s/2$, so each subsequent subset will shift by only one sample. Let the squared deviation from this mean be defined as

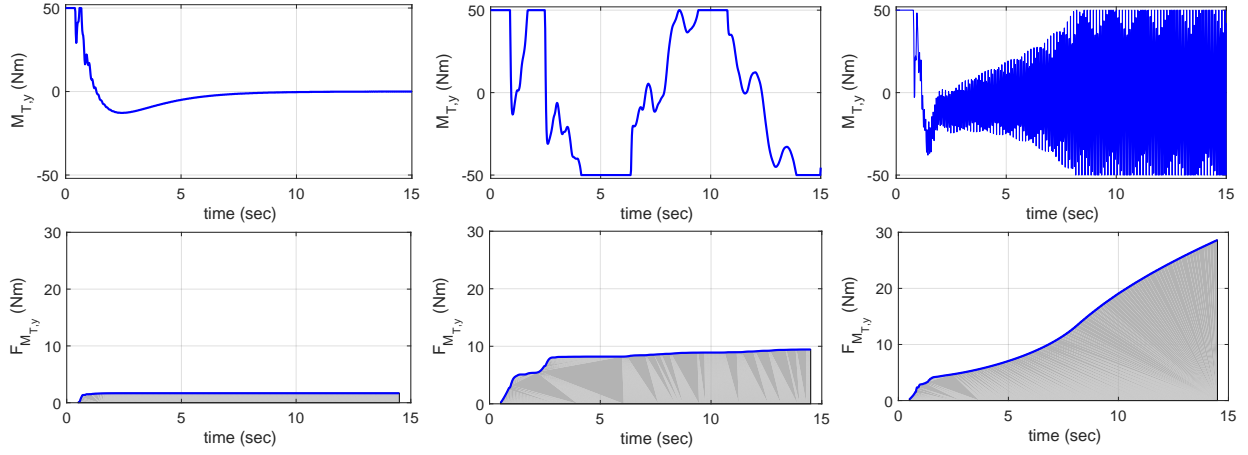American Institute of Aeronautics and Astronautics

Figure 9. Actuator commands and cumulative standard deviation: nominal (left), off-nominal (middle), and unstable (right).

$s_{u,j} = (u_{j+n_s/2} - \bar{y}_j)^2$, which represents the value at the midpoint of subset j. The cumulative standard deviation, F_u, for subset j is then

$$F_{u_j} = \sqrt{\frac{1}{N - n_s - 1} \sum_{k=1}^{j} s_k} \qquad (24)$$

Figure 9 gives three examples of the behaviour of the pitch thrusters, given the step command of $\theta_c = 1°$. In the left two figures, the pitch thruster activity is shown for the nominal response. Due to the discrete change in attitude command, the pitch thrusters exhibit a large jump in required control moment. This discrete jump contributes to a rapid increase in $F_{M_{T,y}}$. The corresponding (grey) surface under the curve, $\sum_{F_{M_{T,y}}} = \int_0^t F_{M_{T,y}}(t)dt$, is a performance measure for these jumps, and should be as small as possible for smoother controls. For an off-nominal design case (the one shown in Fig. 8 and the middle plots of Fig. 9), where the controller performance has purposely been made worse, saturation periods can be discerned, as well as some low-frequency oscillations. Both effects result in a significant increase of $\sum_{F_{M_{T,y}}}$, although the effect of low frequency oscillations is not immediately recognisable. When in doubt, this criterion should be re-evaluated with different subset sample sizes, n_s. Finally, in the right-most two plots, the downgraded controller can no longer properly steer the satellite, and the actuator is rapidly oscillating between the minimum and maximum thrust values. These high-frequency oscillations are shown as a steady increase of $F_{M_{T,y}}$.

From these results it is obvious that by comparing the numerical values of $\sum_{F_{M_{T,y}}}$, conclusions can be drawn towards the control behaviour, even though it paints a *global* picture only. For the examples shown, these values are $\sum_{F_{M_{T,y}}} = 23.1$ Nm s, 113.2 Nm s and 191.1 Nm s, respectively. It may be clear that the *gradient* of $F_{M_{T,y}}$ is indicative of *local* oscillations. It is stressed, though, that the two parameters are indicative only, because both the choice of sample interval and the progression of the mean control value have an effect on the actual values. However, these performance metrics can serve their purpose in an automated procedure to optimise the control-system design. This has been detailed in Ref. 18.

To link the controller performance to the flexible dynamics, an integrated panel deflection can be defined, or alternatively, the integrated motion of a single point (*e.g.,* the panel tip). Focussing on the former, the (absolute) motion of all structural nodes can be tracked over time, and similar to the performance indices defined earlier, three indices can be defined:

$$\sum_{u_x} = \int_0^t \int_0^L |u_x(\mathbf{x})| dx dt \qquad \sum_{u_y} = \int_0^t \int_0^L |u_y(\mathbf{x})| dx dt \qquad \sum_{u_z} = \int_0^t \int_0^L |u_z(\mathbf{x})| dx dt \qquad (25)$$
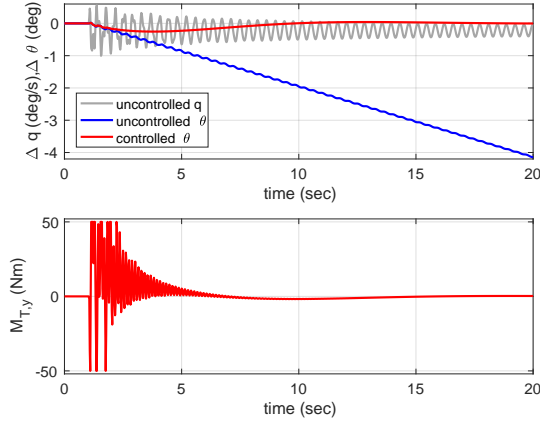
American Institute of Aeronautics and Astronautics

Figure 10. Effect of single tip-impact in Z-direction on pitch motion, uncontrolled and controlled.

where $u(\mathbf{x})$ is representing the (three-dimensional) displacement of a single node, the inner integral representing the total, absolute displacement of all nodes in the panel, and the outer integral determining the effect for the duration of the simulation. The larger the values of these three flexural performance indices, the larger the displacement or the longer the duration the beam is away from the initial position. The subscripts x, y, and z indicate that the three vector components of the displacement vector are treated separately.

C. Impact Analysis

The impact analysis is based on the simulation of an impulsive change in angular momentum due to the impact of a space-debris particle. A mass of 1 g was assumed to impact the solar panel with a relative velocity of 2 km/s in the Z-direction only. Assuming that the linear momentum is transferred in 0.02 s, this implies a force of $F_Z = 100$ N. For the first run, the impact point is taken again at the panel edge on its centreline, yielding a moment arm of 16 m, and a moment of $M_Y = 1,600$ Nm (for the duration of 0.02 s). Due to the momentum transfer, the satellite will start rotating and it is up to the controller to negate that. As explained earlier, no additional commands are given other than to return to zero steady-state. For the controlled simulations with impacts only, the output-error controller discussed in Sec. III.C (Table 4) will be used. Later in this section the effect on space-debris impact during a manoeuvre will also be studied. In that case the complete SAC (Tables 1-3) will be used.

In Fig. 10 the effect of a single debris impact at the tip of the starboard solar panel is shown. Two situations are compared, *i.e.,* uncontrolled and controlled. In the uncontrolled case, the impact creates a moment about the y-axis that results in a non-zero pitch rate, q. As there is no control, the pitch angle θ starts linearly increasing. The "flapping" motion of the solar panel induces a small oscillation in q that is also visible in θ. After 20 s, the satellite has drifted to over 4°. With an active controller, the error in θ remains very small ($\Delta\theta_{max} \approx 0.3°$) and is effectively reduced to zero. However, as the impact causes a spike in q, this causes the controller to saturate, as it has been designed to keep the angular errors very small. The panel oscillations cause a rapid bang-bang-like switching, but after a few seconds the controller manages to stabilise, after which the thruster pulsing becomes smoother. The high-frequency thruster switching does not show in θ, though, which is smooth at all times.

The next step in the analysis is an impact off-centre, *i.e.,* away from the centre line. The panel width of 2.3 m allows for a maximum moment arm of 1.15 m. Assuming $\Delta y = 1$ m, the induced moment is $M_X = 100$ Nm. In combination with $F_Z = 100$ N at the tip, this results in the controlled motion shown in Fig. 11. The simulation is run for 50 s, to show the convergence behaviour and to serve as a benchmark for the Monte-Carlo analyses in the next Sec. IV.D. It was already clear from the previous run that an impact of this magnitude causes some control issues. This is amplified by adding an M_X. Roll control does not suffer from the high-frequency oscillations as the pitch control does – the latter has to control the "flapping" motion of the panels. A maximum error of $\Delta\phi \approx 0.1°$ is induced, and although the roll controller takes some time to stabilise (but with marginal activity), the error is so small that this is not an issue. As before, pitch control is the strongest. The behaviour is the same as before, although it takes a few seconds more until the
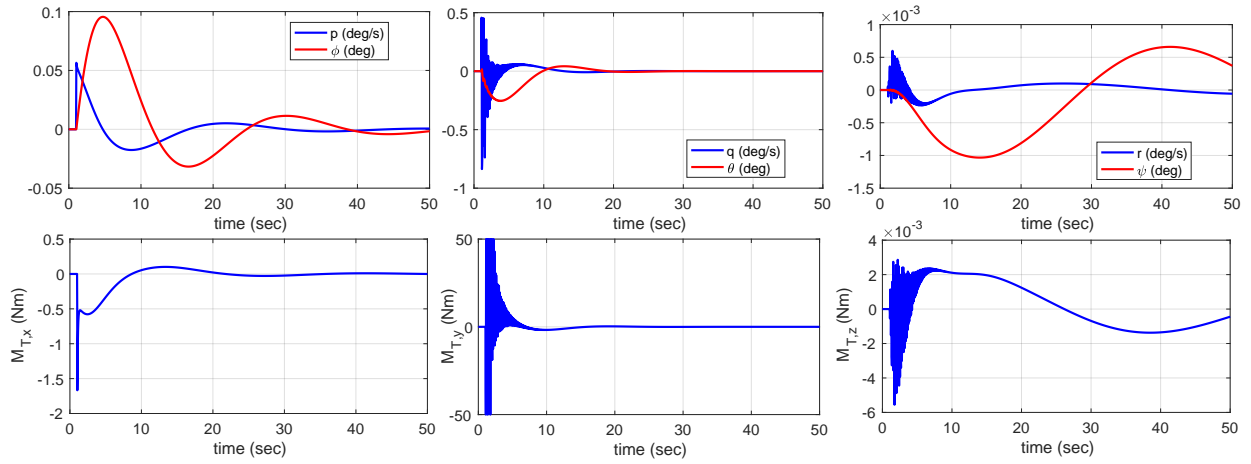
Figure 11. Effect of single tip-impact due to F_Z and M_X on attitude (top) and control effort (bottom).
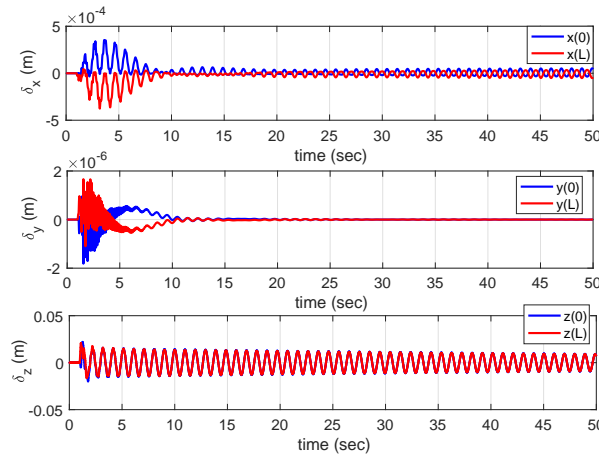

Figure 12. Effect of single tip-impact due to F_Z and M_X on the tip displacement, relative to the satellite bus.

control becomes smooth. The induced θ is somewhat larger and it takes about 20 s before it has effectively reduced to zero. Yaw control is not really required, as the induced angle and thus also the control moment are small. It is noteworthy, though, that the panel flapping also shows as a "vibration" in the z-thruster.

Figure 12 shows the time history of the relative displacement of both panels with respect to the satellite bus, which is also rotating due to the manoeuvres. The δ_x, δ_y, and δ_z refer to the deformation displacement, which is the difference of the total displacement and the rigid body rotation. The oscillations of the deformation are quickly counteracted by the controller, although there is a small steady-state error that corresponds to less than 10% of the accepted pointing accuracy requirement. In addition, it may seem odd that there is residual motion of the flexible panels while the controller does not seem to respond. In fact, this is due to the controller using the angle and angular velocity difference to control the motion of the satellite bus. In the case where both panels are moving exactly symmetrically, there is no total moment, hence no rotation or rotation rate applied at the satellite bus. It may not be desireable from a structural point of view to have this flapping motion, but from a control point of view, the satellite is stabilised. (And indeed, if there is an additional perturbation in the flexible mechanics, the motion will be controlled by the SAC.)

To get an idea about the order of magnitude of the performance indicators introduced in the previous section, they are evaluated for this 50 s run. The runs of the upcoming Monte-Carlo analyses are also set to 50 s, so the current run can serve as a benchmark for comparison.

- Control error: $\sum_{\phi_{err}} = 1.00°$s, $\sum_{\theta_{err}} = 1.58°$s, $\sum_{\psi_{err}} = 0.03°$s.

  The integrated control errors are all relatively small, which was to be expected from the small absolute errors. It is obvious that the (theoretical) minimum error is zero, which cannot be obtained, of course.
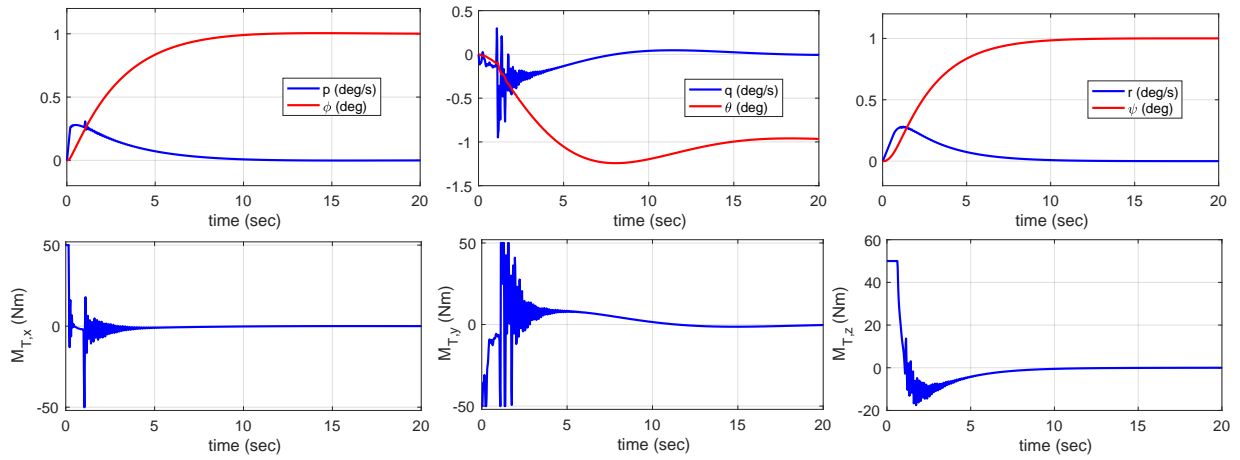
American Institute of Aeronautics and Astronautics

Figure 13. Effect of single tip-impact during manoeuvring on attitude (top) and control effort (bottom).

Errors in the same range will be the result of similar angular offsets as the ones shown in Fig. 11. Significantly larger errors indicate either large overshoots, or a long-duration offset, and might indicate stabilisation problems for the controller.

- Control effort: $\sum_{M_{T,x}} = 3.8$ Nm s, $\sum_{M_{T,y}} = 69.3$ Nm s, $\sum_{M_{T,z}} = 0.06$ Nm s.
  As expected, the integrated control effort of the pitch thruster is the dominating one, and is caused by only 10 s of activity. As the thruster is saturated (maximum moment is 50 Nm), larger values of integrated control effort might indicate longer periods of saturation.

- Oscillatory behaviour: $\sum_{F_{M_{T,x}}} = 2.4$ Nm s, $\sum_{F_{M_{T,y}}} = 250.7$ Nm s, $\sum_{F_{M_{T,z}}} = 0.02$ Nm s.
  The strong oscillations with large amplitudes show as a large value of the oscillatory behaviour of the pitch thruster. In the case this index is a lot larger, it typically means that the thrusters are in a perpetual bang-bang state. Despite the oscillations in the yaw thruster, its index is very small, due to the very small amplitude. The roll thruster index is mainly determined by the single discrete jump at the moment of impact.

- Integrated panel deflection: $\sum_{u_x} = 0.0034$ m s, $\sum_{u_y} = 0.0041$ m s, $\sum_{u_z} = 1.3424$ m s.

  The integrated deflection is quite an abstract parameter that may be difficult to interpret. It is clear, though, that $\sum_{u_z}$ is the largest, which corresponds with the most flexible direction and can be linked with panel flapping. These indices will be used for a relative comparison of the effects of the impacts rather than an absolute one. The large value in the z objective function is due to the relatively larger flapping motion about the y-axis, induced by the impact itself and, possibly, the control moments.

The third run focusses on the effect of debris impact during the execution of a manoeuvre, in this case the combined step functions shown in Fig. 5: $\phi_c = \psi_c = 1°$ and $\theta_c = $ -1° executed at $t = 0$ s. One second after manoeuvre initiation the solar-panel tip is hit by debris ($F_Z = 100$ N, $M_X = 100$ Nm). The effect of this impact is very visible (Fig. 13), but the effect on the controller is not really different from before. Of course, the pitch thruster saturates with bang-bang switching for a few seconds, and also the effects in the roll and yaw thruster are much more noticeable (the roll thruster spikes to saturation once), but this can be explained by the fact that the system is now more dynamic, and therefore more susceptible to the perturbing effect of the impact. The effect on ϕ and ψ is hardly, if at all, noticeable, and the response stays smooth at all times. Even the response of θ is smooth, but due to the impact there is more overshoot of the -1°set point, and it takes about 10 s longer before the set point is reached and stable. All in all, however, the controller deals well with the impact.

The last run in this section assumes two sequential impacts during the manoeuvre, one at $t = 1$ s and one at $t = 6$ s. Both impacts are on the tip of the panel, with $F_Z = 100$ N and $M_X = 100$ Nm (they are independent of the current position of the solar panels). The resulting response is shown in Fig. 14. Of
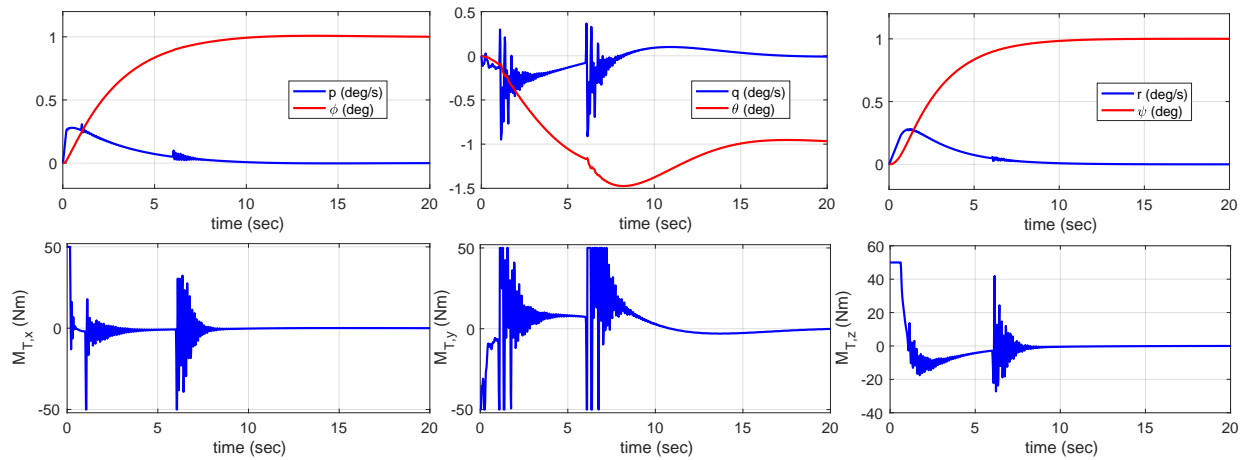
Figure 14. Effect of two tip-impacts during manoeuvring on attitude (top) and control effort (bottom).

course, the first 6 s of the response is identical to the one shown in Fig. 13. After the second impact, θ is significantly influenced, with a maximum error of $\Delta\theta = 0.5°$. The other two angles are not really influenced, but that is not true for the controls. Each thruster exhibits larges, oscillating moments, but the controller is robust enough to overcome these and resumes normal control shortly thereafter.

To conclude this section, space-debris strikes have a significant *impact* on the attitude controller, and a robust controller is required to deal with them. One can debate whether the error margins are perhaps too tight, easily leading to saturation of the actuators. That may be true, but one should also realise that space-debris impact can occur at any time, also when the satellite is in a fine-pointing mode. In the next section, varying the momenta and impact location will be analysed and how those parameters affect the performance indicators evaluated earlier.

D. Sensitivity Analysis

To study the effect of impact strength (combination of the external force and moment, resulting in the change of angular momentum), and the impact location, two Monte-Carlo batches are executed. The first one (500 runs) assumes a single impact at $t = 1$ s, with the three force components F_X, F_Y, and F_Z independently varied in the range of [0, 400] N, the three moment components, M_X, M_Y, and M_Z, in the range of [0, 100] Nm, and the impact location between 2 and 16 m. The second batch (750 runs) assumes two impacts, one at $t = 1$ s as before, and one at $t = 6$ s, for the same location variation, but now with force and moment ranges of [-400,+400] N and [-100,100] Nm, respectively. All parameters are varied according to a uniform distribution.

The results from the first batch are shown in Figs. 15 through 17. Figure 15 shows the integrated control error and integrated control effort. It is clear that roll control is marginally affected by the impacts. Pitch control, on the other hand, has difficulty controlling the satellite under multiple impacts, judging from the fact that the control effort is up to three times larger than for the benchmark. However, with a maximum integrated control error of 6°s (four times larger than the benchmark), it is safe to conclude that the controller keeps the satellite stable in all occasions. A diverging attitude would lead to a much larger value. Yaw control is now also a lot more active compared to the benchmark, but that is logical given the forces and moments acting in all directions. However, the integrated control error is less than half the one for θ, although there is a significant control effort required to keep this error small. The control effort is comparable with the one for the pitch thruster. In Fig. 16 the oscillatory behaviour of the thrusters is shown, or in other words, the amount of "bang-bang switching" behaviour that was observed in Sec. IV.C. It is interesting to see that the roll and pitch thruster seem to suffer less from the impacts, now that a simultaneous, three-direction momentum transfer takes place. Coupling between the three axes somehow has a stabilising effect, so for a worst-case scenario, impact in a single direction should be considered. The yaw thruster exhibits many more oscillations, but in the benchmark it was hardly active. There is a second peak observed, which is likely centred around a particular combination of large forces and/or moments. Figure 17 shows the integrated beam deflections in three directions. On average, the distributions are more or less the same (and large),

American Institute of Aeronautics and Astronautics

which is, in fact surprising given the different stiffnesses for each of the axes. This is something to be studied in more detail at a later point. It suffices to say that there is a lot going on with the panels, which requires a more thorough structural analysis. Finally, looking at the simulation results of the individual runs confirms that larger forces closer to the tip, as well as larger moments, induce larger errors and require more thruster effort to counteract.

The results of the second Monte-Carlo batch are shown in Figs. 18 through 20. The integrated control error for ϕ, Fig. 18, seems also to be impervious to the second impact, which is, in fact no surprise as the second impact is similar to the first one. Also ψ is not so much affected, although the integrated error is somewhat larger. The pitch angle, on the other hand, shows many more larger errors, with a maximum error that is almost double the one from the first batch. Still, if one realises that when a constant error of $0.1°$ is present for the full run of 50 s this means that $\sum_{\theta_{err}} = 5°$s. So, an error of $20°$s could be caused by an average error of $0.4°$, which does not sound so bad. However, what is more troublesome is the control effort. The results are split into two groups, with the larger group having an almost ten times larger control effort (note that an error of 2,000 Nm s can be caused by 40 s (=80%) of maximum thrust). This seems to indicate large periods of saturation and/or strong oscillatory behaviour. This is, in fact, confirmed by Fig. 19: a similar group distribution, with the larger group exhibiting significant oscillations. Of course, it can be debated whether two sequential impacts are realistic to happen. If so, then there might actually be other reasons to worry than just the satellite's controllability and stability. The final Fig. 20 shows the same result as in Fig. 17: an equal motion over the three axes, albeit with a 60% increase.

This second batch was intended to push the limits in capability of the controller. Although the SAC appears to be robust and can relatively easily deal with actuator saturation, having to deal with two sequential, large-momentum impacts is too much, but given the limited actuator range of ±50 Nm this is probably true for any control system.

V.   Conclusions and Recommendations

An impact resulting in a moment of $M_Y = 1,600$ Nm was simulated on an uncontrolled and controlled Rosetta-like spacecraft. The impact created a non-zero pitch rate, which in the uncontrolled case causes the satellite to drift over $4°$ after 20 s. The controlled motion for the impact on the x-axis caused a maximum error in θ of only $\Delta\theta \approx 0.3°$ and was nullified after approximately 10 s, and although the controller initially exhibited bang-bang switching oscillations, it stabilised after a few seconds. In the case of the impact causing an additional rolling moment of 100 Nm, the control was effected so that the θ error remained the same, and an error of $\phi \approx 0.1°$ was observed. Some residual motion in the flexible solar panels was noted, but the motion is symmetric about the satellite bus and does not induce an angular change (or rate) in the bus itself, and does not require any control effort.

Impact simulations were run for a single impact during a manoeuvre and for two consecutive impacts during a manoeuvre. In both cases, there was a noticeable effect of the impact on the controller moments; although the effect was hardly noticed in the ϕ and ψ response. The thrusters did saturate with bang-bang switching for a few seconds and the effects were now greater in the roll and yaw thrusters than the non-manoeuvring case, because the system was dynamic and more sensitive to perturbing forces.

Monte-Carlo simulations were run in batches of 500, to study the effect of the impact strength and impact location on the response of the spacecraft. A second set of Monte-Carlo simulations were performed in batches of 750, and with different force and moment ranges, to determine the effects of two consecutive impacts on the spacecraft response. The roll control was only marginally affected by the variation of impact momentum, and pitch control, expectedly had up to four times the effort than the benchmark. Interestingly, coupling between the three axes was noted to have a stabilising effect during the three-direction momentum transfers. The roll and pitch thrusters suffered less from the impacts, but the yaw thruster exhibited more oscillation than the benchmark, primarily because in the benchmark it was hardly active. In the batches with sequential impacts, the control error was reasonable, if one examined only the average error over the full simulation time; however, the control effort was up to ten times greater than the single-impact simulations, which included large periods of saturation and strong oscillatory behaviour.

Some of the future work will revolve around the improvement of the beam model, without resorting to higher-complexity models, and determining the robustness of a nonlinear model that will allow the development of larger rotations than the current linear model. Such a nonlinear model would be useful to compare with a fully nonlinear continuum model, which was presented in previous works by the authors. Also the use
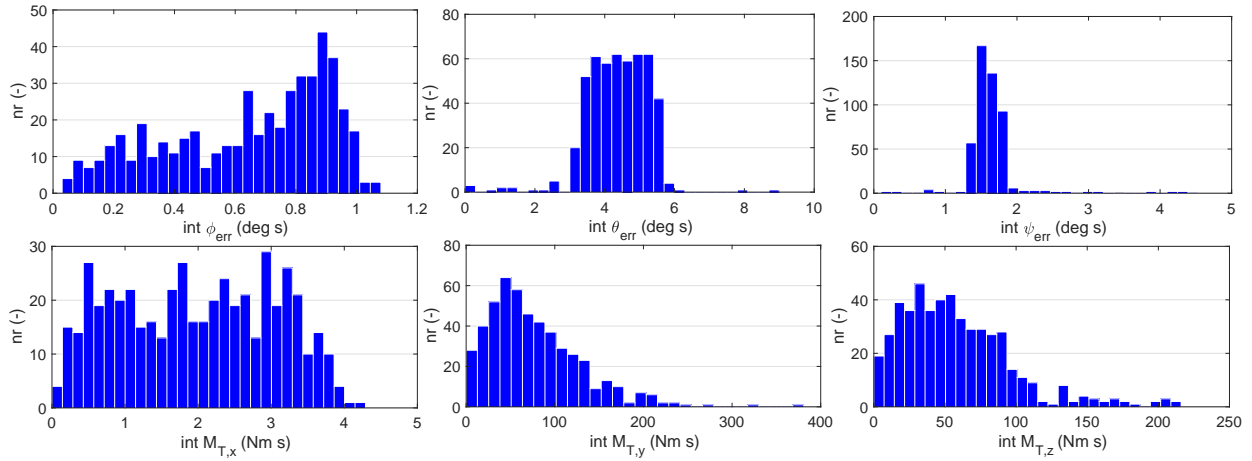
American Institute of Aeronautics and Astronautics

Figure 15. Integrated control errors (top) and control effort (bottom) for varying impact conditions (single event at $t = 1$ s).
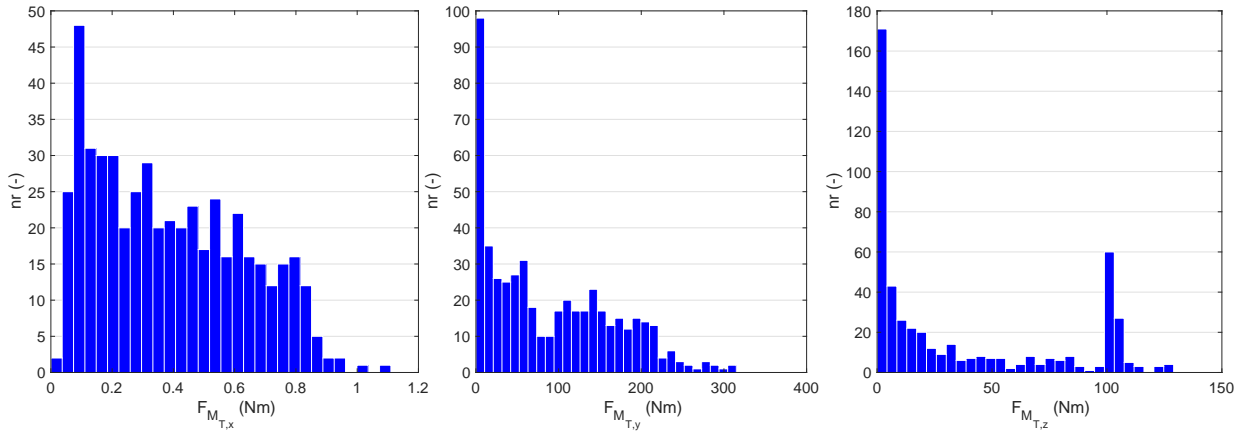

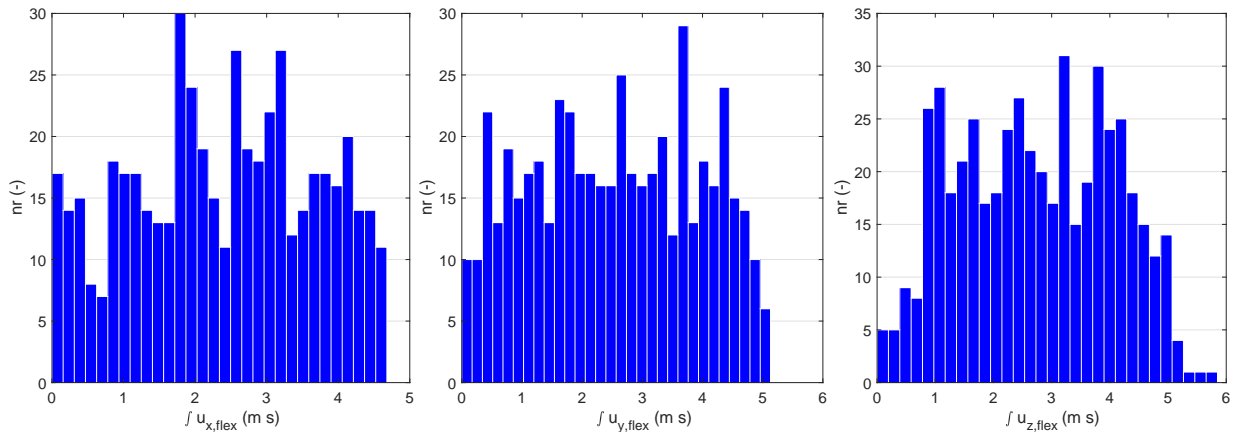**Figure 16. Oscillatory behaviour for varying impact conditions (single event at $t = 1$ s).**

Figure 17. Integrated panel deflection for varying impact conditions (single event at $t = 1$ s).

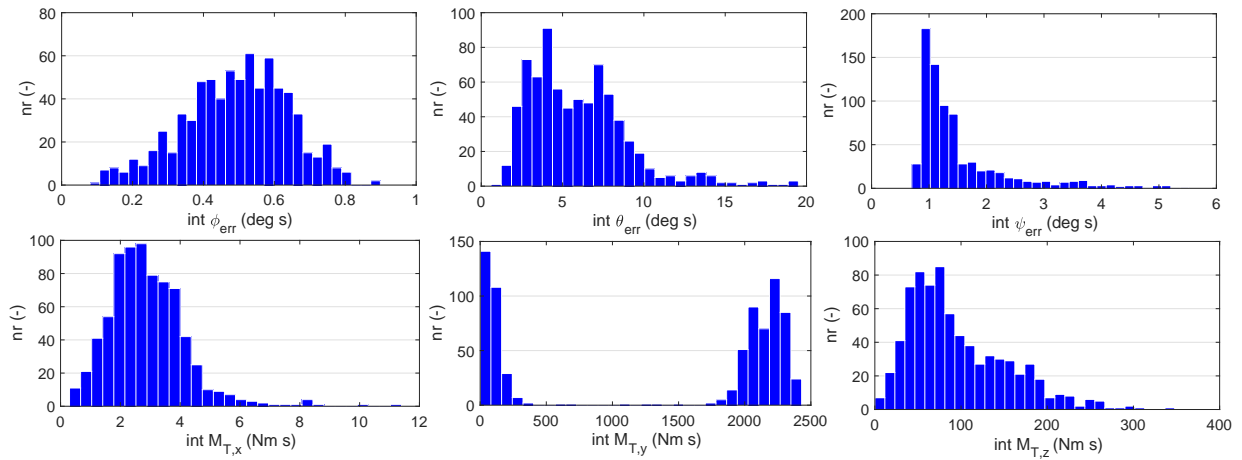American Institute of Aeronautics and Astronautics

Figure 18. Integrated control errors (top) and control effort (bottom) for varying impact conditions (two events at $t = 1$ s and $t = 6$ s).
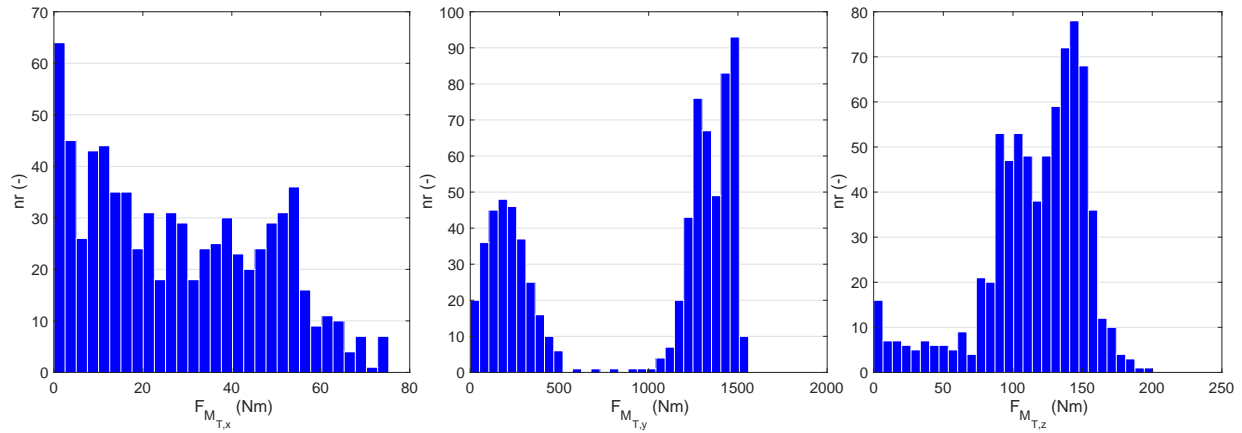

Figure 19. Oscillatory behaviour for varying impact conditions (two events).
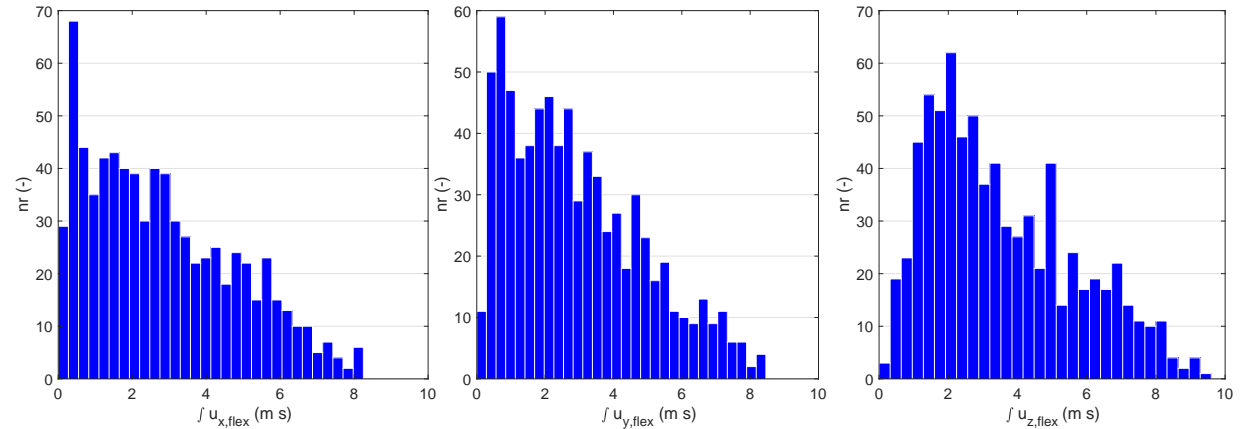

Figure 20. Integrated panel deflection for varying impact conditions (two events).

of a Runge-Kutta integration should be considered to reduce the numerical issues. With a model that can accurately incorporate large rotations, one could examine more complex manoeuvres and develop control strategies for capture operations, faster autonomous manipulator movement, or collision avoidance with or-

bital debris. With respect to controller design, the performance-optimisation methodology should be further developed, and linked with actual design requirements.

References

[1]Kaufman, H., Barkana, I. and Sobel, K., *Direct adaptive control algorithms: Theory and applications*, Second edition, Springer-Verlag, New York, 1998.

[2]Barkana, I. and Guez, A., "Simple adaptive control for a class of non-linear systems with application to robotics", *International Journal of Control*, Vol. 52, No. 1, 1990.

[3]Barkana, I., "Classical and Simple Adaptive Control for Non-Minimum Phase Autopilot Design", *Journal of Guidance, Control, and Dynamics*, Vol. 24, No. 4, pp. 631-638, July-August 2004.

[4]Mehiel, E.A. and Balas, M.J., "Adaptive Control for a Deployable Optical Telescope", AIAA-2004-5222, From: *AIAA Guidance, Navigation, and Control Conference*, Providence, RI, August 16-19, 2004.

[5]Mooij, E., "Adaptive Heat-Flux Tracking for Re-entry Guidance", AIAA-2014-4142, *AIAA/AAS Astrodynamics Specialist Conference*, San Diego, CA, August 4-7, 2014.

[6]Mooij, E. and Wijnands, Q.G.J., "Real-Time Implementation of a Model Reference Adaptive Control System", AIAA-03-5754, *AIAA Simulation and Modelling Technologies Conference*, Austin, TX, August 11-14, 2003.

[7]Gili, P. *et al.*, "Articulated and Flexible Multibody Satellite Dynamics Modelling", 20th *AIAA International Communications Satellite Systems Conference and Exhibit*, 2002.

[8]Zhang, M.-J., and Zhao, C.-Y., "Attitude stability of a spacecraft with two flexible solar arrays on a stationary orbit around an asteroid subjected to gravity gradient torque", *Astrophysics Space Science*, Vol. 351, pp. 507-524.

[9]Gasbarri, P., Monti, R., Sabatini, M., "Very large space structures: Non-linear control and robustness to structural uncertainties", *Acta Astronautica*, Vol. 93, 2013, pp. 252-265.

[10]Gasbarri, P., Monti, R., De Angelis, C. Sabatini, M., "Effects of uncertainties and flexible dynamic contributions on the control of a spacecraft full-coupled model", *Acta Astronautica*, Vol. 94, 2014a, pp. 81-97.

[11]Gasbarri, P., Sabatini, M., Leonangeli, N., and Palmerini, G., "Flexibility issues in discrete on-off actuated spacecraft: Numerical and experimental tests", *Acta Astronautica*, Vol. 101, 2014b, pp. 515-526.

[12]Gransden, D., Bornemann, P. B., Rose, M., Nitzsche, F., "A Constrained Generalised-α method for coupling rigid parallel chain kinematics and elastic bodies", *Journal of Computational Mechanics*, Vol. 55, 2015, pp. 527-541.

[13]Gransden, D.I. and Mooij, E., "Simple Adaptive Control of a Satellite with Large Flexible Appendages", IAC-16-C1.8.8.x35217, 67th *International Astronautical Congress*, Guadalajara, Mexico, September 26-30, 2016.

[14]Simeon, B., "On Lagrange multipliers in flexible multibody dynamics",*Computational Methods in Applied Mechanical and Engineering*, Vol. 195, 2006, pp. 6993-7005.

[15]Ferreira, A. J. M., *MATLAB Codes for Finite Element Analysis: Solids and Structures*, Springer, Dordrecht, The Netherlands, 2009.

[16]Oñate, E., *Structural analysis with the finite element method. Linear statics: volume 2: beams, plates and shells*, Springer Science & Business Media, 2013.

[17]Mooij, E., "Passivity Analysis for Non-Linear, Non-Stationary Entry Capsules", *Int. J. Adapt. Control Signal Processing*, Published Online 2013.

[18]Mooij, E. and Gransden, D.I., "Model Verification of a Satellite with Large Flexible Appendages for Control System Design", AIAA-2018-0209, *2018 AIAA SciTech Forum: Dynamics and Control of Large Space Structures and Tethers*, Kissimmee, FL, 8-12 January 2018.

[19]Gopal, M., *Modern Control System Theory*, Wiley Eastern Ltd., New Delhi, Second Reprint, June 1989.